frontiers | Frontiers in Built Environment

TYPE Original Research
PUBLISHED 17 December 2024
DOI 10.3389/fbuil.2024.1477804

EDITED BY
Cheng Fang,
Tongji University, China

REVIEWED BY
James Michael Ricles,
Lehigh University, United States
Baiping Dong,
Tongji University, China

*CORRESPONDENCE
Wei Song,
✉ wsong@eng.ua.edu

RECEIVED 08 August 2024
ACCEPTED 26 November 2024
PUBLISHED 17 December 2024

CITATION
Ruiz S and Song W (2024) Adaptive compensation for multi-axial real-time hybrid simulation via nonlinear parameter estimation.
Front. Built Environ. 10:1477804.
doi: 10.3389/fbuil.2024.1477804

Adaptive compensation for multi-axial real-time hybrid simulation via nonlinear parameter estimation

Santiago Ruiz and Wei Song*

Department of Civil, Construction and Environmental Engineering, The University of Alabama, Tuscaloosa, AL, United States

For Real-time hybrid simulation (RTHS) to be stable and accurate, it is essential to address the time desynchronization issue between the numerical and physical substructures. Desynchronization is primarily caused by time delays, inherent dynamics of the control plant, system uncertainties, and noises. While existing adaptive compensators have shown effective tracking performance in single-input single-output (SISO) RTHS, their effectiveness in multi-input multi-output (MIMO) RTHS has not been fully demonstrated. MIMO-RTHS presents additional challenges due to its larger solution space, and significant dynamic coupling between actuators. To address these challenges, this study introduces an adaptive compensation framework for MIMO-RTHS. The proposed framework utilizes a control law based on the inverse dynamics of the control plant, incorporating real-time adaptive parameter updates through Extended Kalman Filter (EKF) and Unscented Kalman Filter (UKF) methods. Both the transfer function (TF) and discrete-time state-space (SS) models of the plant are employed in distinct parameter estimation cases. The performance of the proposed compensation is validated through a multi-axial RTHS (maRTHS) benchmark problem. Extensive simulations on the maRTHS incorporating various earthquake inputs, sensor noise, and model uncertainties, demonstrated an excellent tracking performance and strong robustness across four parameter estimation cases (EKF-TF, UKF-TF, EKF-SS, and UKF-SS). The use of UKF with SS model (UKF-SS) achieved superior performance, effectively managing nonlinearities and noise without requiring low-pass filtering.

KEYWORDS

real-time hybrid simulation, MIMO control, adaptive compensation, actuator tracking, uncertainty, hydraulic actuator, extended Kalman filter, unscented Kalman filter

1 Introduction

Real-time hybrid simulation (RTHS) is an experimental technique to perform dynamic evaluation of complex structural systems (Nakashima et al., 1992). This technique divides the emulated structure into two parts: the numerical substructure (NS), which is simulated by a computer program, and the physical substructure (PS), which is tested in a laboratory. The interface between the NS and the PS is imposed by a transfer system (e.g., servo hydraulic actuator) in real-time. The transfer system along with the PS is often refer to as the control plant. While RTHS offers a cost-effective and spatially economical alternative to traditional structural tests (Gomez et al., 2014), it faces a critical issue of desynchronization at the NS-PS interface. This issue can cause significant experimental errors or even failure, impacting the accuracy and stability of RTHS (Darby et al., 1999; Horiuchi et al., 1999; Zhao et al., 2003). A primary cause of desynchronization is "actuator time delay" or simply "time delay", which originates from the closed-loop nature of RTHS, inherent dynamics of the control plant, and data acquisition limitations (Hayati and Song, 2017; Hayati and Song, 2018). This issue is further exacerbated by system modeling uncertainties (Silva et al., 2020), and process and measurement noises (Song and Dyke, 2013; Song, 2018; Song et al., 2020).

To mitigate the desynchronization issue, numerous compensation strategies have been developed. Traditional strategies assume constant time delay and rely on pre-estimations of system parameters. These strategies include polynomial extrapolation (Horiuchi et al., 1999; Nakashima and Masaoka, 1999; Darby et al., 2002), phase lead compensation (Zhao et al., 2003; Jung et al., 2007), and inverse compensation (Chen et al., 2009; Chen and Ricles, 2009). However, in RTHS, time delays are not constant due to frequency-dependent uncertainties in actuator dynamics and specimen characteristics (Dyke et al., 1995; Darby et al., 2002; Hayati and Song, 2017; Hayati and Song, 2018). Consequently, traditional compensation strategies fall short when dealing with significant system uncertainties (Silva et al., 2020; Condori Uribe et al., 2023). Recently, adaptive compensation strategies have gained considerable attention due to their ability to dynamically adjust their parameters in real-time, responding to changes and uncertainties in the system (Chae et al., 2013; Chen et al., 2015; Ouyang et al., 2019).

Parameter estimation method is a popular and effective adaptive control approach, and it has already been introduced into RTHS compensation domain. Chae et al. (2013) developed the adaptive time series (ATS) compensation, which updates the coefficients of a transfer system using the least squares (LS) method for single-input single-output (SISO) RTHS. Palacio-Betancur and Gutierrez Soto (2019) extended this method by implementing recursive least squares (RLS) for parameter estimation in SISO-RTHS. Further studies by Wang et al. (2020) and Ning et al. (2022) explored adaptive control schemes for SISO-RTHS based on discrete system models with time-varying coefficients using the LS method, while Ning et al. (2020) implemented Kalman filter (KF) as the parameter estimator. To enhance the robustness of adaptive control in SISO-RTHS, nonlinear parameter estimators, such as the Extended Kalman Filter (EKF) and Unscented Kalman Filter (UKF) have been employed. The EKF linearizes the system around the current estimate to handle nonlinearities, while the UKF uses a deterministic sampling approach to capture the mean and covariance more accurately (Wan and Van Der Merwe, 2000). The computational efficiency, ability to provide timely updates, and robustness against nonlinearities and noises of EKF and UKF, make these estimators suitable for real-time nonlinear model updating (Song and Dyke, 2013; Song and Dyke, 2014). Strano and Terzo (2016) developed an adaptive compensation scheme based on EKF, to continuously adjust system parameters, enhancing the accuracy and stability of hydraulic actuator control in RTHS. Huang et al. (2023) and Wang et al. (2024) investigated adaptive compensation with UKF, exhibiting good robustness.

Despite the demonstrated effectiveness of adaptive control using nonlinear parameter estimation methods in SISO-RTHS, its application to multi-input multi-output (MIMO) RTHS remains unverified. The transition from SISO- to MIMO-RTHS enables the simulation of more realistic loading scenarios and complex structural responses; however, it introduces unique challenges. In MIMO-RTHS, control actions applied to one actuator can affect responses in other actuators due to interdependencies across the MIMO control plant, creating cross-coupling effects that prevent the direct application of existing SISO strategies. Furthermore, the development of MIMO-RTHS involves a higher level of complexities than the SISO counterparts, including a larger and more intricate solution space, complex actuator kinematics, and increased computational demand (Mercan et al., 2009; Condori Uribe et al., 2023; Najafi et al., 2023). To address these challenges and achieve effective compensation, this study presents a robust adaptive compensation strategy for MIMO-RTHS, validated through a multi-axial RTHS (maRTHS) benchmark problem (Condori Uribe et al., 2023). The contributions of this work are twofold: (*i*) the development of a comprehensive adaptive compensation framework based on nonlinear parameter estimations (EKF and UKF), which provides a systematic approach for MIMO-RTHS; (*ii*) the system formulation for parameter estimation, which considers the control plant in two commonly-adopted dynamic system models, namely the transfer function (TF) and the discrete-time state-space (SS) models, resulting in four distinct parameter estimation cases: EKF-TF, UKF-TF, EKF-SS, and UKF-SS. The proposed framework allows for implementation flexibility and performance comparison among the different estimation techniques and system formulations. Through a comparative study using the maRTHS benchmark problem (Condori Uribe et al., 2023), it is shown that the proposed compensation framework can account for the interactions and dependencies between multiple inputs and outputs, effectively managing the dynamic coupling between actuators during MIMO-RTHS.

The remainder of this paper is organized as follows. Section 2 presents the proposed adaptive compensation methodology. Section 3 details the implementation and results of the virtual maRTHS. Finally, Section 4 summarizes the main findings and conclusions of this research.

2 Methodology

In this section, the proposed adaptive compensation framework for MIMO-RTHS is presented, to mitigate the desynchronization between the NS and PS, such that the output of the control plant tracks the "*desired*" (or "*target*") signals. This compensator employs a control law based on the inverse dynamics of the control plant, which aims to cancel the plant dynamics. Thus, the control plant model is a key aspect for the formulation of the presented methodology. This work explores two distinct models of the control plant: (a) a transfer function model; (b) a discrete-time state-space model. Both models are utilized for parameter estimation in distinct cases. However, only the transfer function model is used during the command generation (control law).

2.1 Control plant

2.1.1 Transfer function model

The control plant that comprises the PS in a MIMO problem can be generally represented by a matrix of transfer functions (TFs) as,

$$\mathbf{H}(s) = \begin{bmatrix} H_{11}(s) & \cdots & H_{1j}(s) \\ \vdots & \ddots & \vdots \\ H_{i1}(s) & \ldots & H_{ij}(s) \end{bmatrix} \tag{1}$$

where s denotes the Laplace variable, and $H_{ij}(s)$ is the ij-th transfer function entry for the different input (j)-output (i) pairs of $\mathbf{H}(s)$. Each transfer function $H_{ij}(s)$ is a fraction with a numerator polynomial $N_{ij}(s)$ and a denominator polynomial $D_{ij}(s)$, expressed in factored form as,

$$H_{ij}(s) = \frac{N_{ij}(s)}{D_{ij}(s)} = \frac{b_{ij,0}\left(s - z_{ij,1}\right)\left(s - z_{ij,2}\right)\ldots\left(s - z_{ij,n_{ij}}\right)}{a_{ij,0}\left(s - p_{ij,1}\right)\left(s - p_{ij,2}\right)\ldots\left(s - p_{ij,m_{ij}}\right)} \tag{2}$$

where $b_{ij,0}$ and $a_{ij,0}$ are scaling coefficients, $z_{ij,k}$ (for $k = 1, 2, \ldots, n_{ij}$) and $p_{ij,l}\left(\text{for}\, l = 1, 2, \ldots, m_{ij}\right)$ are respectively the zeros and poles of the transfer function, which generally can be identified through a system identification process. Note that, to ensure that the system is physically realizable, the transfer function $H_{ij}(s)$ must be proper, i.e., the order of the numerator polynomial must be less than or equal to the order of the denominator polynomial ($n_{ij} \leq m_{ij}$).

In this work, the zeros and poles from Equation 2 are expressed as a parameter vector, $\boldsymbol{\theta}$. According to the benchmark problem definition (Condori Uribe et al., 2023), uncertainties, represented as $\Delta\boldsymbol{\theta}$, are introduced to $\boldsymbol{\theta}$ due to model imprecisions in the control plant. These uncertainties effectively modify the transfer function matrix in Equation 1 as $\mathbf{H}(s|\boldsymbol{\theta}, \Delta\boldsymbol{\theta})$.

2.1.2 Discrete-time state-space model

The identified transfer function of the plant from Equation 1 can be used to obtain a state-space (SS) realization in discrete time as,

$$\mathbf{z}_{k+1} = \mathbf{A}(\boldsymbol{\theta})\mathbf{z}_k + \mathbf{B}(\boldsymbol{\theta})\mathbf{u}_k \tag{3}$$

$$\mathbf{x}_k = \mathbf{C}(\boldsymbol{\theta})\mathbf{z}_k + \mathbf{D}(\boldsymbol{\theta})\mathbf{u}_k \tag{4}$$

where $\mathbf{A}, \mathbf{B}, \mathbf{C}$, and $\mathbf{D}$ are the state-space matrices derived in terms of the plant parameters $\boldsymbol{\theta}$; $\mathbf{z}_k$ is the state vector at time step k, determined by the chosen realization; $\mathbf{u}_k$ is the system input, i.e., the command signal sent to the plant; and $\mathbf{x}_k$ is the plant output. Here, $\boldsymbol{\theta}$ follows the same definition from Equation 2, along with the associated uncertainties, $\Delta\boldsymbol{\theta}$.

2.2 Adaptive compensation framework

While adaptive control schemes have been developed for SISO-RTHS (e.g., Strano and Terzo (2016), Huang et al. (2023)), they have yet to be applied in MIMO-RTHS. In this work, the proposed adaptive compensation framework is realized for coupled MIMO systems, such as those presented in Equations 1–4, accounting for system uncertainties ($\Delta\boldsymbol{\theta}$) and capturing cross-coupling effects between actuators. A typical maRTHS scheme incorporating the proposed adaptive compensation framework is shown in Figure 1. The input signal to the system (i.e., external force), is denoted by $\boldsymbol{F}_{ext}$; the restoring force vector from the experimental substructure is denoted as $\boldsymbol{f}_m$; the desired and measured signal vectors are $\mathbf{x}_d$ and $\mathbf{x}_m$, respectively; $\mathbf{u}_c$ is the command signal vector; and the control plant is represented in Laplace domain as $\mathbf{H}(s|\boldsymbol{\theta}, \Delta\boldsymbol{\theta})$ [as shown in Section 2.1]. Hereafter, the control plant is simply denoted as $\mathbf{H}(s)$.

The collection of blocks (I), (II), and (III) in Figure 1 generates the control law, which is realized by utilizing the inverse dynamics of the control plant derived from the transfer function in Equation 1. The control law incorporates adaptive parameters that are estimated by block (IV) at each time step. The parameter estimation process is described in Section 2.3. The remainder of this section explains the control generation process.

The transfer function matrices $\mathbf{H}(s)$ and $\mathbf{G}(s)$ relate the desired signal $\mathbf{x}_d$ to the command $\mathbf{u}_c$ and the measured signal $\mathbf{x}_m$ as follows,

$$\boldsymbol{X}_m = \mathbf{H}(s)\boldsymbol{U}_c \tag{5}$$

$$\boldsymbol{U}_c = \mathbf{G}(s)\boldsymbol{X}_d \tag{6}$$

where $\boldsymbol{X}_m$, $\boldsymbol{X}_d$, and $\boldsymbol{U}_c$ denote the signals $\mathbf{x}_m$, $\mathbf{x}_d$, and $\mathbf{u}_c$ in Laplace domain, respectively. From Equation 5 and Equation 6, it can be seen that the plant dynamics are cancelled when $\mathbf{G}(s) = \mathbf{H}^{-1}(s)$, leading to the measured signal matching the desired signal ($\boldsymbol{X}_m = \boldsymbol{X}_d$). However, a direct inverse of $\mathbf{H}(s)$ results in improper transfer functions for $\mathbf{G}(s)$ (Carrion et al., 2009; Phillips et al., 2014). To compute this inverse effectively, the proposed compensator makes use of the time derivatives of the desired signal. First, a common denominator polynomial of $\mathbf{H}(s)$ is found and denoted as $\Delta(s)$. The polynomial $\Delta(s)$ incorporates poles and zeros from each actuator (2 actuators in this benchmark problem–see Section 3.1), capturing the coupling dynamics in the MIMO system. Then, by introducing $\boldsymbol{X}_m = \boldsymbol{X}_d$ and $\mathbf{G}(s) = \mathbf{H}^{-1}(s)$, Equation 5 can be rewritten as,

$$\boldsymbol{X}_d = \mathbf{G}^{-1}(s)\boldsymbol{U}_c = \frac{1}{\Delta(s)}\tilde{\mathbf{H}}(s)\boldsymbol{U}_c \tag{7}$$

where $\tilde{\mathbf{H}}(s) = \Delta(s)\mathbf{H}(s)$, and thanks to $\Delta(s)$, the ij-th entry of $\tilde{\mathbf{H}}(s)$, $\tilde{H}_{ij}(s)$, is a polynomial rather than a fraction and its inverse can be properly realized. It should be noted that the output in Equation 7 is now considered as $\boldsymbol{X}_d$, under the assumption that the desired and measured signals match ($\boldsymbol{X}_m = \boldsymbol{X}_d$). Further manipulation of Equation 7 yields the command signal vector $\boldsymbol{U}_c$ to the plant, expressed as,

$$\boldsymbol{U}_c = \mathbf{R}\left(s|\hat{\boldsymbol{\theta}}_k\right)\Delta(s)\boldsymbol{X}_d(s) = \mathbf{R}\left(s|\hat{\boldsymbol{\theta}}_k\right)\boldsymbol{\Psi}_d \tag{8}$$

where $\mathbf{R}\left(s|\hat{\boldsymbol{\theta}}_k\right) = \tilde{\mathbf{H}}^{-1}(s)$ is a matrix of transfer functions that can be properly realized. The term $\Delta(s)\boldsymbol{X}_d(s)$ is realized in the time domain by computing the function $\boldsymbol{\psi}_d = \mathbf{g}\left(\boldsymbol{\gamma}, \hat{\boldsymbol{\theta}}_k\right)$, shown as the block (II) in Figure 1, where $\boldsymbol{\gamma} = \left(\mathbf{x}_d, \dot{\mathbf{x}}_d, \ddot{\mathbf{x}}_d, \ldots\right)$ denotes the collection of the time derivatives of $\mathbf{x}_d$ [see block (I)]. The number of required time derivatives is determined by the order of the polynomial $\Delta(s)$. $\hat{\boldsymbol{\theta}}_k$ denotes the estimated plant parameters at time step k, and $\boldsymbol{\Psi}_d$ denotes the Laplace transform of the signal $\boldsymbol{\psi}_d$.

The presented approach addresses the issue of improper transfer functions in $\mathbf{G}(s)$ and facilitates the command generation. The

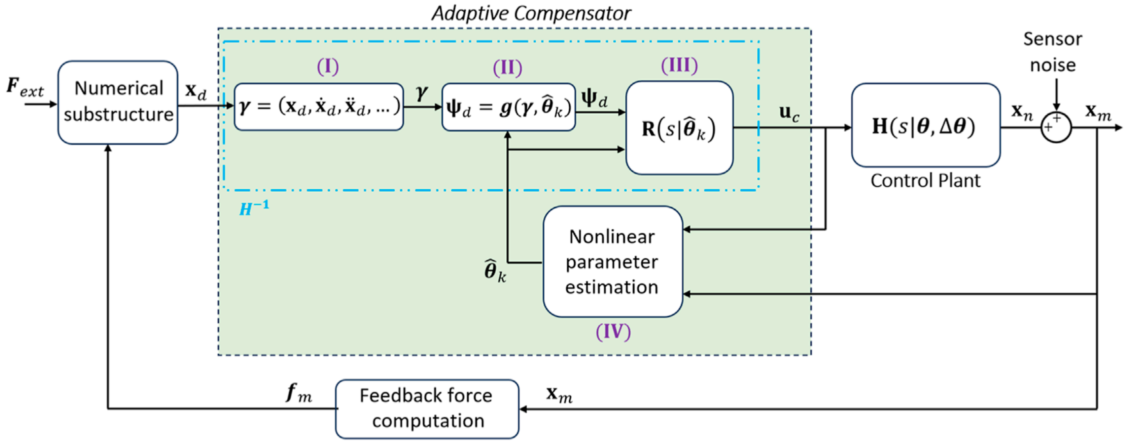

FIGURE 1
maRTHS scheme and proposed adaptive compensator.

following section describes the parameter estimation process for the updating of the plant poles and zeros ($\hat{\theta}$) used in the control law of Equation 8.

2.3 Nonlinear parameter estimation

The physical domain of RTHS is subject to disturbances such as imprecisions in experimental setup, unmodeled process and dynamics (e.g., friction), and process and measurement noises, which introduce uncertainties to the plant ($\Delta\theta$) during RTHS, as indicated in Section 2.1. To address the desynchronization issues caused by these uncertainties, this work employs online parameter estimation to update the plant parameters in real-time during the command generation. As observed from the two control plant formulations from Equations 1, 2 (for the TF model) and Equations 3, 4 (for the discrete-time SS model), the system formulations are nonlinear with respect to θ. Therefore, nonlinear estimators, EKF and UKF, are employed to estimate θ with the two introduced control plant models (see Section 2.1).

Both EKF and UKF are formulated for a general discrete-time system model expressed as,

$$\textit{State transition}: \; \boldsymbol{\phi}_k = \mathbf{f}(\boldsymbol{\phi}_{k-1}, \boldsymbol{\mu}_{k-1}) + \mathbf{w}_{k-1} \tag{9}$$

$$\textit{Observation model}: \; \mathbf{y}_k = \mathbf{h}(\boldsymbol{\phi}_k, \boldsymbol{\mu}_k) + \mathbf{v}_k \tag{10}$$

where $\mathbf{f}(\boldsymbol{\phi}_{k-1}, \boldsymbol{\mu}_{k-1})$ is the process function; $\boldsymbol{\phi}_k$ is the state vector; $\boldsymbol{\mu}_k$ is the system input vector; $\mathbf{w}_k$ is a white noise with zero mean and covariance matrix $\mathbf{Q}$; $\mathbf{y}_k$ is the system output vector; $\mathbf{h}(\boldsymbol{\phi}_k, \boldsymbol{\mu}_k)$ is the observation function; and $\mathbf{v}_k$ is a white noise with zero mean and covariance matrix $\mathbf{R}$. It should be noted from Equations 9, 10, that both process and measurement noises are considered as additive in this work.

Depending on the plant model employed for the application of EKF or UKF, the corresponding estimation system models are explained below.

a) Transfer function model

For the control plant in transfer function (TF) form, the state vector and process function at time step k in Equations 9, 10 are defined as the plant parameters at that time step, resulting in the following state transition function,

$$\underbrace{\boldsymbol{\theta}_k}_{\boldsymbol{\phi}_k} = \underbrace{\boldsymbol{\theta}_{k-1}}_{\mathbf{f}(\boldsymbol{\phi}_{k-1}, \boldsymbol{\mu}_{k-1})} + \underbrace{\mathbf{w}_{k-1}^{\mathrm{TF}}}_{\mathbf{w}_{k-1}} \tag{11}$$

The observation function is set as the command signal $\mathbf{u}_c$ to the control plant. Therefore, Equation 10 becomes,

$$\underbrace{\mathbf{u}_{c,k}}_{\mathbf{y}_k} = \underbrace{\tilde{\mathbf{u}}_{c,k}\left(\boldsymbol{\theta}_k, \gamma_{\mathbf{x}_m}\right)}_{\mathbf{h}(\boldsymbol{\phi}_k, \boldsymbol{\mu}_k)} + \underbrace{\mathbf{v}_k^{\mathrm{TF}}}_{\mathbf{v}_k} \tag{12}$$

In this formulation, the nonlinearity arises from Equation 12, where the computation of the system output vector $\mathbf{u}_{c,k}$ ($\mathbf{u}_c$ at the k-th time step) involves the polynomial expansion of the plant poles and zeros, as described in Section 2.2 (Equation 8). Note that $\tilde{\mathbf{u}}_{c,k}$ denotes the observation function for $\mathbf{u}_{c,k}$, and $\mathbf{w}_k^{\mathrm{TF}}$ and $\mathbf{v}_k^{\mathrm{TF}}$ are the additive noise vectors for the state vector (i.e., parameter $\boldsymbol{\theta}_k$) and observation vector (i.e., command signal $\mathbf{u}_{c,k}$), respectively. Additionally, unlike in Section 2.2 where $\mathbf{x}_d$ is used to calculate $\mathbf{u}_c$, the parameter estimation step utilizes the measured signal $\mathbf{x}_m$ and its respective time derivatives $\gamma_{\mathbf{x}_m}$ [i.e.,; $\gamma_{\mathbf{x}_m} = (\mathbf{x}_m, \dot{\mathbf{x}}_m, \ddot{\mathbf{x}}_m, \dots)$].

b) Discrete-time state-space model

When the discrete-time state-space (SS) model of the control plant is used for parameter estimation, the original states of the system from Equations 3, 4 are augmented with the parameters that need to be estimated. Thus, the state transition and observation functions for the augmented discrete-time SS model are formulated as,

$$\underbrace{\mathbf{z}_{\mathbf{a}k}}_{\boldsymbol{\phi}_k} = \underbrace{\mathbf{A}_{\mathbf{a}k-1}(\boldsymbol{\theta}_{k-1})\mathbf{z}_{\mathbf{a}k-1} + \mathbf{B}_{\mathbf{a}k-1}(\boldsymbol{\theta}_{k-1})\mathbf{u}_{c,k-1}}_{\mathbf{f}(\boldsymbol{\phi}_{k-1}, \boldsymbol{\mu}_{k-1})} + \underbrace{\mathbf{w}_{k-1}^{\mathrm{SS}}}_{\mathbf{w}_{k-1}} \tag{13}$$

$$\underbrace{\mathbf{x}_{m,k}}_{\mathbf{y}_k} = \underbrace{\mathbf{C}_{\mathbf{a}k}(\boldsymbol{\theta}_k)\mathbf{z}_{\mathbf{a}k} + \mathbf{D}_{\mathbf{a}k}(\boldsymbol{\theta}_k)\mathbf{u}_{c,k}}_{\mathbf{h}(\boldsymbol{\phi}_k, \boldsymbol{\mu}_k)} + \underbrace{\mathbf{v}_k^{\mathrm{SS}}}_{\mathbf{v}_k} \tag{14}$$

where $\mathbf{z}_{\mathbf{a}_k}$ is the augmented state vector at the k-th time step, i.e., $\mathbf{z}_{\mathbf{a}k} = [\mathbf{z}_k, \boldsymbol{\theta}_k]^T$, of dimension $(p+n)$, with p and n being the

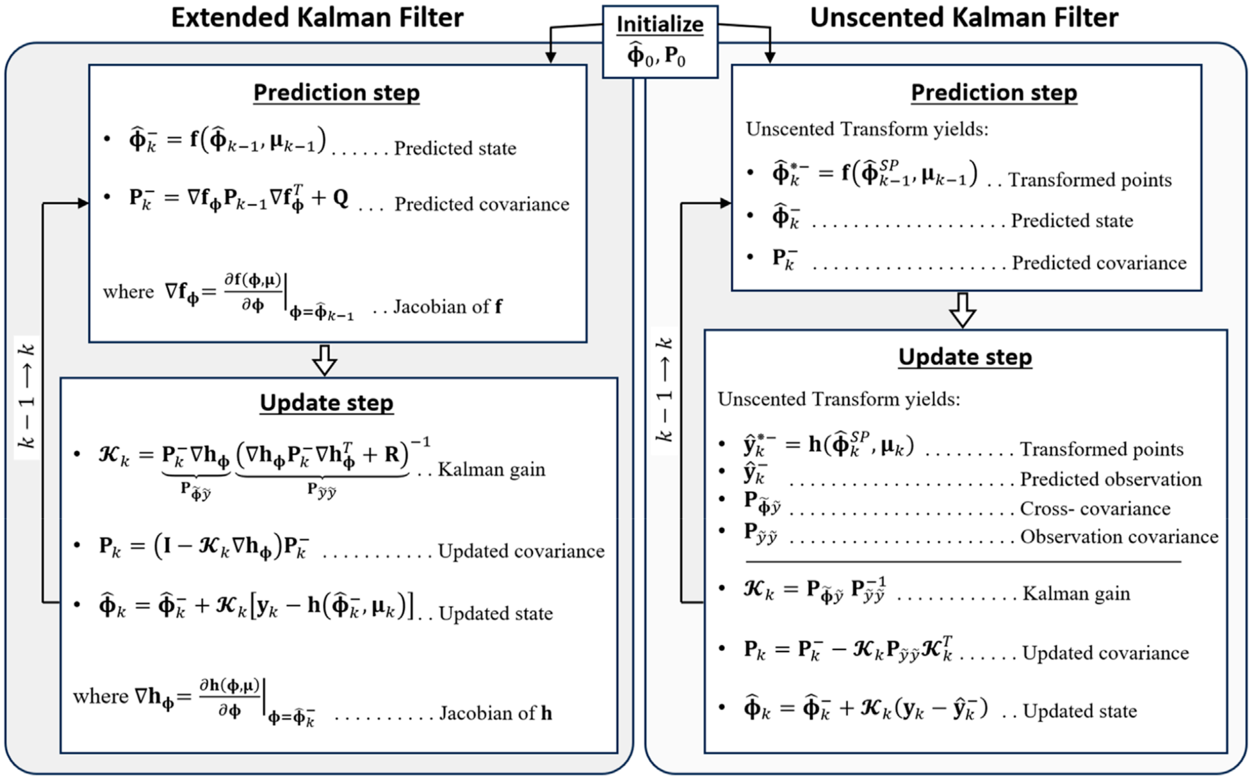

FIGURE 2
EKF and UKF state estimation.

dimensions of the original state-space vector $\mathbf{z}_k$, and the parameter vector $\boldsymbol{\theta}_k$, respectively. The input and output system vectors correspond to the command and measured signals $\mathbf{u}_{c,k}$ and $\mathbf{x}_{m,k}$. The additive noise vectors for $\mathbf{z}_{\mathbf{a}_k}$ and $\mathbf{x}_{m,k}$ are denoted as $\mathbf{w}_k^{\mathrm{SS}}$ and $\mathbf{v}_k^{\mathrm{SS}}$, respectively. $\mathbf{A}_{\mathbf{a}_k}$, $\mathbf{B}_{\mathbf{a}_k}$, $\mathbf{C}_{\mathbf{a}_k}$, and $\mathbf{D}_{\mathbf{a}_k}$ are the augmented state-space matrices at the k-th time step, computed using the forward Euler method as,

$$\mathbf{A}_{\mathbf{a}_k}(\boldsymbol{\theta}) = \mathbf{I}_{(p+n)\times(p+n)} + \Delta t \cdot \begin{bmatrix} A(\boldsymbol{\theta})_{p\times p} & \mathbf{0}_{p\times n} \\ \mathbf{0}_{n\times p} & \mathbf{0}_{n\times n} \end{bmatrix} \tag{15}$$

$$\mathbf{B}_{\mathbf{a}_k}(\boldsymbol{\theta}) = \Delta t \cdot \begin{bmatrix} \mathbf{B}(\boldsymbol{\theta})_{p\times h} \\ \mathbf{0}_{n\times h} \end{bmatrix} \tag{16}$$

$$\mathbf{C}_{\mathbf{a}_k}(\boldsymbol{\theta}) = \begin{bmatrix} \mathbf{D}(\boldsymbol{\theta})_{h\times p} & \mathbf{0}_{h\times n} \end{bmatrix} \tag{17}$$

$$\mathbf{D}_{\mathbf{a}_k}(\boldsymbol{\theta}) = \mathbf{D}(\boldsymbol{\theta})_{h\times h} \tag{18}$$

where Δt is the sampling time of the RTHS, and h is the dimension of $\mathbf{u}_{c,k}$ or $\mathbf{x}_{m,k}$, which is assumed to be the same. This formulation introduces the nonlinearity through the dependence of the state-space matrices on $\boldsymbol{\theta}_k$, as indicated in Equations 13–18.

Regardless of the selected system model (TF or SS), both EKF and UKF can be applied for parameter estimation. The estimation methods are depicted in Figure 2 utilizing the general system formulation of Equations 9, 10.

EKF and UKF are extensions of the standard Kalman filter, designed to handle nonlinear systems (Song, 2011). Both methods consist of two recursive steps: the prediction step and the update step, as shown in Figure 2. In the prediction step, the process function $\mathbf{f}$ is used to predict the prior state estimate ($\hat{\boldsymbol{\phi}}_k^-$) and its covariance ($\mathbf{P}_k^-$). In the update step, this prediction is updated by incorporating the observation function $\mathbf{h}$ to obtain the posterior state estimate ($\hat{\boldsymbol{\phi}}_k$) and its covariance ($\mathbf{P}_k$), while minimizing the mean square error of the estimates with the Kalman gain $\mathcal{K}_k$. The details for the implementing EKF and UFK algorithms are omitted here, but can be found in (Song, 2011; Song and Dyke, 2013; Song and Dyke, 2014).

The primary difference between these estimation methods lies in handling the nonlinearities of the process and observation functions. The EKF approximates the nonlinear functions by linearizing them around the current state estimate using a first-order Taylor series expansion, which involves calculating their respective Jacobians $\nabla\mathbf{f}_{\boldsymbol{\phi}}$ and $\nabla\mathbf{h}_{\boldsymbol{\phi}}$ (see Figure 2). The calculation of the Jacobians is omitted here for succinctness. In contrast, UKF uses a deterministic sampling scheme known as the Unscented Transform (UT) to generate a set of "*sigma points*" that capture the mean (e.g., $\hat{\boldsymbol{\phi}}_k^-$) and covariance of the state distribution (e.g., $\mathbf{P}_k^-$) without the Jacobian calculations (Julier, 2002). The sigma points, indicated in Figure 2 with the superscript "*SP*", are carefully chosen to accurately reflect the state distribution. These sigma points are directly propagated through the nonlinear functions, resulting in transformed points $\hat{\boldsymbol{\phi}}_k^{*-}$ and $\hat{\mathbf{y}}_k^{*-}$ for the state and output, respectively. The mean and covariance of the predicted state and observation are then computed as a weighted sum of their

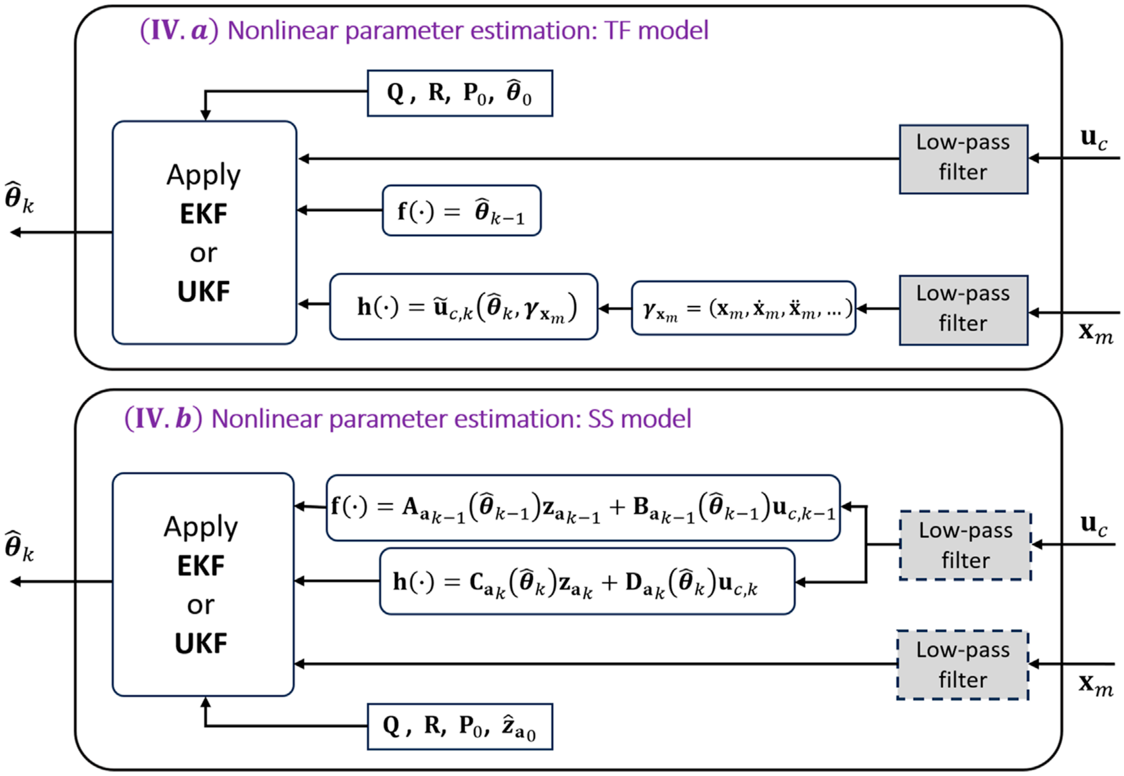

FIGURE 3
maRTHS nonlinear parameter estimation cases.

respective transformed sigma points (Wan and Van Der Merwe, 2000). Additionally, both EKF and UKF require an initialization of the state and covariance, indicated in Figure 2 as $\hat{\phi}_0$ and $\mathbf{P}_0$, respectively, along with the selection of appropriate covariances $\mathbf{Q}$ and $\mathbf{R}$, which involves a search process (Song et al., 2017; Song, 2018).

By replacing the general system formulation of Equations 9, 10 in Figure 2 with the selected control plant formulations from Equations 11, 12 (for the TF model) or Equations 13, 14 (for the discrete-time SS model), four (4) parameter estimation cases can be obtained: EKF-TF, UKF-TF, EKF-SS, and UKF-SS. These cases are illustrated in Figure 3, showing the architecture inside of block IV from Figure 1.

As shown in Figure 3, the same low-pass filter is applied to the signals $\mathbf{u}_c$ and $\mathbf{x}_m$. The low-pass filter is indicated with dashed lines in block (IV.*b*) because this work also explores the option of not applying low-pass filtering for the SS model case (see Section 3.4). A difference between the TF and SS approaches is the definition of the system input and output vectors, $\boldsymbol{\mu}_k$ and $\mathbf{y}_k$. In the TF model (see Equations 11, 12), the input is $\gamma_{\mathbf{x}_m}$ [i.e.,; $\gamma_{\mathbf{x}_m} = (\mathbf{x}_m, \dot{\mathbf{x}}_m, \ddot{\mathbf{x}}_m, \ldots)$], which is related to the measured displacement of the plant $\mathbf{x}_m$ and its time derivatives, and the output is the command signal $\mathbf{u}_c$. In contrast, the SS model (see Equations 13, 14) swaps the two with $\mathbf{u}_c$ as the input and $\mathbf{x}_m$ as the output, and therefore without the need for its time derivatives.

3 Results

3.1 maRTHS benchmark problem

The proposed methodology is applied to the maRTHS benchmark developed by Condori Uribe et al. (2023), which provides a virtual RTHS (vRTHS) platform that allows the implementation of customized compensators. In this benchmark problem a three-story, three-bay moment resisting frame is subjected to seismic base excitation corresponding to scaled ground acceleration records of El Centro 1940, Kobe 1995, and Morgan Hill 1984. The central frame of the structure (one-story, one-bay, simply supported) acts as the experimental substructure (see Figure 4), and the remaining structure is the numerical substructure. Displacement and rotational degrees of freedom (DOFs) are used as target signals at the NS-PS interface (control node). These DOFs are refer to as "*frame coordinates*", and are represented in Figure 4 as $\psi_{es,28}$ and $\psi_{es,4}$, where the subscripts 28 and 4 denote the corresponding rotational and translational DOFs defined by Condori Uribe et al. (2023). The NS-PS connection is accomplished through a transfer system that consists of two hydraulic actuators and a steel coupler (see Figure 4). The coupler transfers the linear displacement of the two actuators to produce the desired frame coordinates. The desired and measured actuator linear displacement vectors are referred to as "*actuator coordinates*". Thus, a coordinate transformation is performed during the simulation to transition between these two coordinate systems.

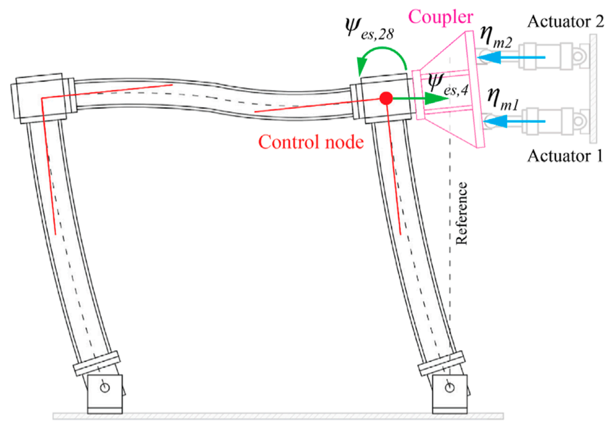

FIGURE 4
Experimental substructure. Adapted from Condori Uribe et al. (2023).

The virtual RTHS is run with a fixed sampling frequency of 1,024 Hz (i.e., the sampling period $\Delta t = 0.976\,\text{ms}$).

In this work, the compensation is performed in the actuator coordinates domain. Therefore, the desired signal is specified as $\mathbf{x}_d = [\eta_{n1} \quad \eta_{n2}]^T$, where η_{n1} and η_{n2} denote the desired linear displacements for actuators 1 and 2, respectively. The command signal is set as $\mathbf{u}_c = [u_1 \quad u_2]^T$, where u_1 and u_2 correspond to the linear displacement commands to actuators 1 and 2, respectively. Likewise, the measured signal is indicated as $\mathbf{x}_m = [\eta_{m1} \quad \eta_{m2}]^T$, where η_{m1} and η_{m2} denote the measured linear displacements of actuators 1 and 2, respectively, as shown in Figure 4.

The control plant model for the maRTHS benchmark problem is given as Equation 19,

$$\mathbf{H}(s) = \begin{bmatrix} H_{11} & H_{12} \\ H_{21} & H_{22} \end{bmatrix} \tag{19}$$

where the subscripts represent the input-output pairs for actuator 1 and actuator 2, respectively. Specifically, u_1 and u_2 are the inputs to the system, while η_{m1} are η_{m2} are the outputs. The adaptive compensator is designed considering the nominal plant model identified by Condori Uribe et al. (2023), which has the following transfer functions,

$$H_{11}(s) = \frac{K_{11}(s+B_1)(s+B_2)}{(s+A_1)(s+A_2)(s+C_1+C_2j)(s+C_1-C_2j)} \tag{20}$$

$$H_{12}(s) = \frac{K_{12}(s+P_1)}{(s+D_1)(s+D_2)(s+C_1+C_2j)(s+C_1-C_2j)} \tag{21}$$

$$H_{21}(s) = \frac{K_{21}(s+B_1)(s+B_2)}{(s+A_1)(s+A_2)(s+C_1+C_2j)(s+C_1-C_2j)} \tag{22}$$

$$H_{22}(s) = \frac{K_{12}(s+P_2)}{(s+D_1)(s+D_2)(s+C_1+C_2j)(s+C_1-C_2j)} \tag{23}$$

From Equations 20–23, C_1, and C_2 denote the poles of the numerical substructure; B_1, B_2, P_1, and P_2 represent the zeros of the transfer functions of the transfer system (i.e., actuators and steel coupler); A_1, A_2, D_1, and D_2 denote the poles of the transfer functions of the transfer system; and K_{11}, K_{12}, K_{21}, and K_{22} are the corresponding transfer function gains.

TABLE 1 Tuned EKF and UKF parameters for maRTHS Benchmark Problem.

Parameter estimation scenario	P_0	Q	R
EKF-TF	$\mathbf{I}_{10\times10}$	$10^{-5}\cdot\mathbf{I}_{10\times10}$	$10^{-1}\cdot\mathbf{I}_{2\times2}$
UKF-TF	$\mathbf{I}_{10\times10}$	$10^{-4}\cdot\mathbf{I}_{10\times10}$	$10^{1}\cdot\mathbf{I}_{2\times2}$
EKF-SS	$\mathbf{I}_{22\times22}$	$\mathbf{0}_{22\times22}$	$10^{-3}\cdot\mathbf{I}_{2\times2}$
UKF-SS	$\mathbf{I}_{22\times22}$	$10^{-11}\cdot\mathbf{I}_{22\times22}$	$10^{-1}\cdot\mathbf{I}_{2\times2}$

3.2 Parameter estimation settings

The parameters in Equations 20–23 are updated in real-time during RTHS, while the transfer function gains are considered as constants. This approach results in the definition of $\boldsymbol{\theta}$, as shown in Equation 24.

$$\boldsymbol{\theta} = [A_1 \quad A_2 \quad B_1 \quad B_2 \quad C_1 \quad C_2 \quad P_1 \quad P_2 \quad D_1 \quad D_2]^T \tag{24}$$

Once the control plant model $\mathbf{H}(s)$ and the nominal parameter $\boldsymbol{\theta}^*$ are established, the four parameter estimation cases are formulated as described in Section 2.3.

As indicated in Section 2.3, a search process is performed to select the initial values of $\hat{\boldsymbol{\phi}}_0$ and $\mathbf{P}_0$, and the covariances $\mathbf{Q}$ and $\mathbf{R}$. The details of the search are omitted here but readers can refer to (Song, 2011; Song et al., 2017; Song, 2018) for more information. This search process may not guarantee to yield the optimal selection, and other search methods can be also considered. The selected EKF and UKF parameters (covariances) are presented in Table 1.

In addition to the covariances presented in Table 1, scaling parameters used during the sigma points computation in UKF were adjusted to enhance the estimation performance. The values for these scaling parameters are set as follows: $\alpha = 0.4$, $\kappa = 0$, and $\beta = 2$. Details on how these parameters influence the sigma points distribution can be found in Wan and Van Der Merwe (2000) and Song (2011).

3.3 Adaptive compensator performance in maRTHS

The proposed adaptive compensator is validated through the vRTHS platform in MATLAB/Simulink R2023b (Mathworks, 2024). The performance is evaluated with a set of 10 performance criteria defined in Condori Uribe et al. (2023). Performance indices (PI), $J_{n,m}$, are utilized for each criterion, where n indicates the criteria number and m depends on the type of evaluation. For example, PIs from $J_{1,m}$ to $J_{4,m}$ evaluate the tracking performance in actuators coordinates (m denotes the actuator number). PIs $J_{5,m}$ and $J_{6,m}$ indicate the tracking performance in frame coordinates (m denotes the DOFs of the control node). PIs from $J_{7,m}$ and $J_{10,m}$ indicate the global RTHS performance, which seek to minimize the error between the reference structure response and the hybrid system response (m denotes the DOFs of the control node and upper stories levels). Lower PIs values indicate better compensation performance,

TABLE 2 Evaluation criteria of maRTHS subjected to 0.4 scaled El Centro Earthquake (1,000 simulations).

Performance criteria		PI $J_{n,m}$	Units	BM-LQG	EKF–TF		UKF–TF		EKF–SS		UKF–SS	
					Mean	SD	Mean	SD	Mean	SD	Mean	SD
Tracking control	Time delay	$J_{1,1}$	ms	2.0	0.00	0.05	0.41	0.88	0.00	0.00	0.00	0.00
		$J_{1,2}$	ms	2.9	0.00	0.00	0.47	0.51	0.00	0.00	0.00	0.00
	Normalized tracking error	$J_{2,1}$	%	4.8	2.71	0.05	3.16	0.40	2.87	0.02	2.68	0.02
		$J_{2,2}$	%	9.4	1.48	0.04	1.79	0.16	1.68	0.02	1.42	0.01
	Max. peak tracking error	$J_{3,1}$	%	5.3	2.50	0.26	3.55	0.75	2.91	0.26	2.45	0.22
		$J_{3,2}$	%	10.3	1.62	0.22	2.07	0.42	1.99	0.16	1.76	0.16
Estimation	Time delay	$J_{4,1}$	ms	1.9	0.00	0.05	0.41	0.88	0.00	0.00	0.00	0.00
		$J_{4,2}$	ms	2.9	0.00	0.00	0.47	0.51	0.00	0.00	0.00	0.00
	Normalized estimation error	$J_{5,4}$	%	6.7	1.85	0.03	2.18	0.18	2.06	0.01	1.82	0.01
		$J_{5,28}$	%	17.8	1.17	0.21	1.79	0.62	1.03	0.08	0.85	0.03
	Max. peak estimation error	$J_{6,4}$	%	7.4	1.82	0.21	2.43	0.50	2.30	0.18	1.93	0.18
		$J_{6,28}$	%	18.8	1.57	0.49	2.34	0.49	1.38	0.18	1.61	0.10
Global RTHS Performance	Normalized RTHS error	$J_{7,4}$	%	10.6	9.69	0.06	9.69	0.34	9.61	0.01	10.00	0.01
		$J_{7,28}$	%	16.8	7.38	0.06	7.34	0.52	7.80	0.01	7.96	0.01
	Normalized RTHS error at upper levels	$J_{8,2}$	%	1.8	6.86	0.05	7.31	0.33	7.38	0.03	7.19	0.01
		$J_{8,26}$	%	3.4	6.19	0.08	6.67	0.25	6.63	0.04	6.40	0.01
		$J_{8,3}$	%	2.1	6.51	0.06	6.97	0.30	7.01	0.03	6.80	0.01
		$J_{8,27}$	%	3.0	6.24	0.07	6.71	0.26	6.70	0.04	6.48	0.01
	Max. peak RTHS error	$J_{9,4}$	%	11.9	8.12	0.36	9.28	0.55	7.93	0.14	8.16	0.15
		$J_{9,28}$	%	18.1	5.89	0.29	6.02	0.26	6.00	0.11	6.13	0.05
	Max. peak RTHS error at upper levels	$J_{10,2}$	%	1.8	5.16	0.12	5.55	0.25	5.59	0.04	5.48	0.02
		$J_{10,26}$	%	2.7	5.05	0.14	5.43	0.21	5.45	0.04	5.36	0.02
		$J_{10,3}$	%	1.8	5.01	0.12	5.41	0.25	5.46	0.04	5.35	0.02
		$J_{10,27}$	%	2.4	5.08	0.13	5.44	0.23	5.50	0.04	5.40	0.02

TABLE 3 Average simulation time for each earthquake input case (1,000 simulations).

Scaled earthquake input [duration (s)]	EKF–TF	UKF–TF	EKF–SS	UKF–SS
El Centro [41.2 s]	7.7	42.7	2.6	28.8
Kobe [50.9 s]	9.4	52.1	7.8	35.3
Morgan [40.0 s]	3.0	68.4	2.8	27.7

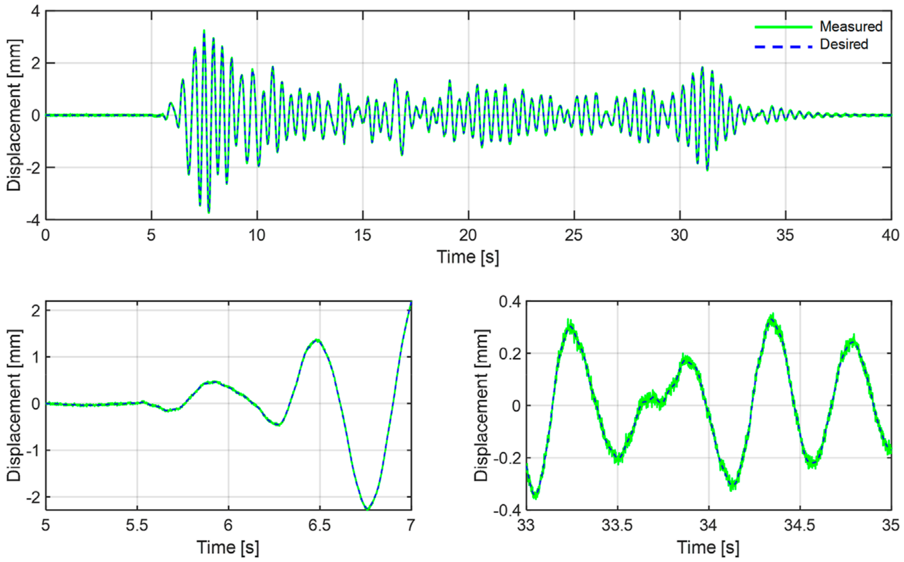

FIGURE 5
maRTHS tracking performance in actuator coordinates (actuator 1) for UKF-SS case with the largest $J_{2,1}$ (0.4 scaled El Centro Earthquake as input).

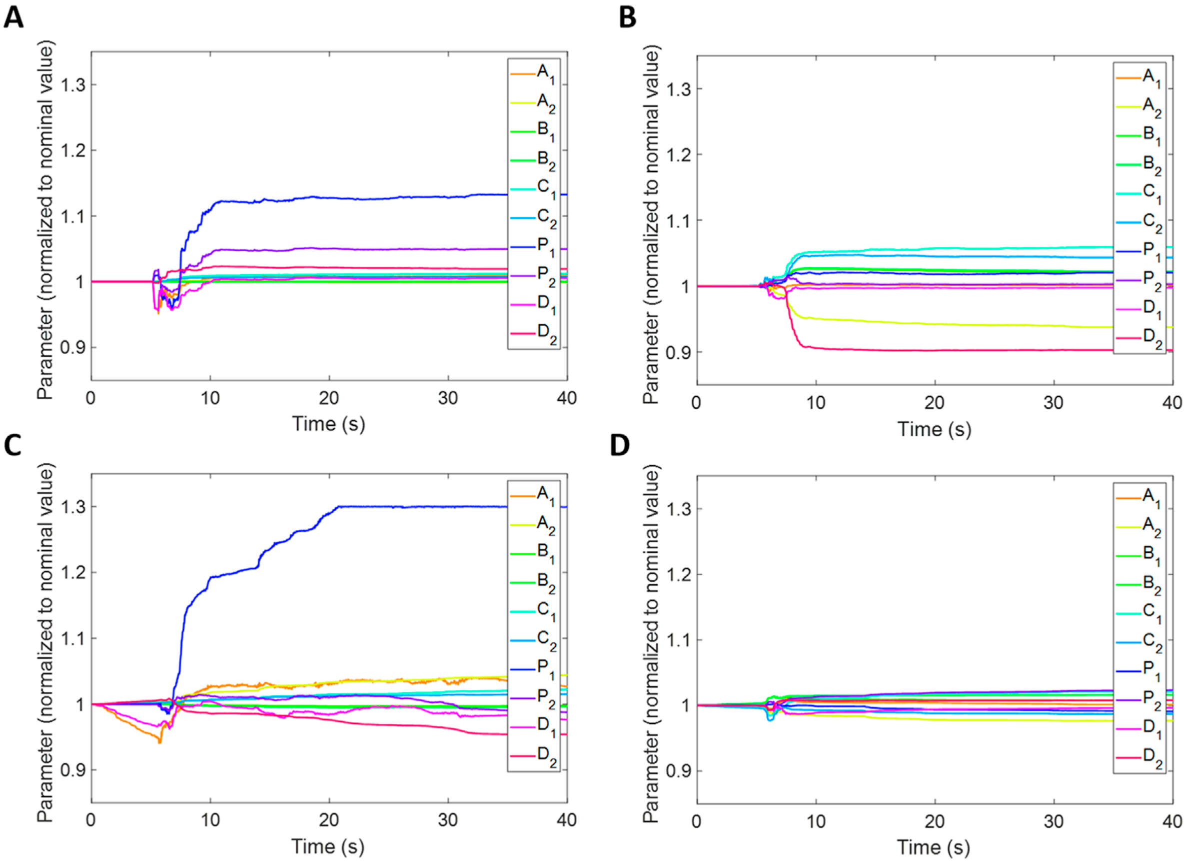

FIGURE 6
Parameter tracking with 0.4 scaled El Centro Earthquake as input and control plant with uncertainties. **(A)** EKF-SS **(B)** UKF-SS. **(C)** EKF-TF **(D)** UKF-TF.

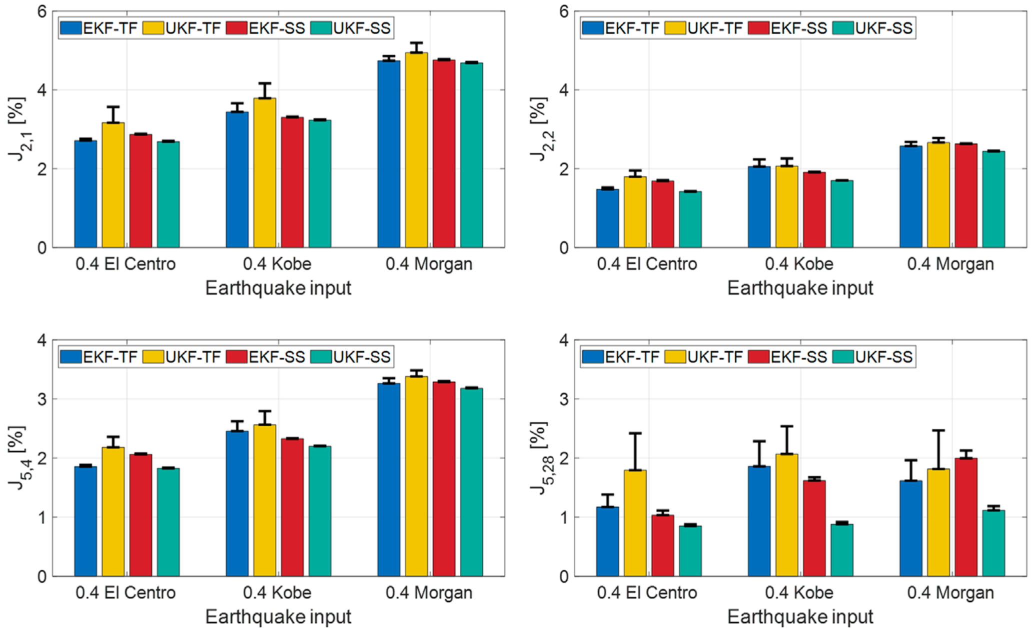

FIGURE 7
Tracking performance in actuator and frame coordinates for all input earthquakes. Mean PIs obtained from 1,000 simulations for each earthquake input.

TABLE 4 Tracking performance criteria of maRTHS subjected to 0.4 scaled El Centro Earthquake (1,000 simulations)–SS formulation without low-pass filter.

Performance criteria		PI $J_{n,m}$	Units	EKF–SS (No low-pass)		UKF–SS (No low-pass)	
				Mean	SD	Mean	SD
Tracking control	Time delay	$J_{1,1}$	ms	1.55	20.70	0.00	0.00
		$J_{1,2}$	ms	−0.38	9.58	0.00	0.00
	Normalized tracking error	$J_{2,1}$	%	7.65	27.64	2.76	0.02
		$J_{2,2}$	%	3.03	7.98	1.64	0.01
	Max. peak tracking error	$J_{3,1}$	%	15.64	54.54	2.64	0.22
		$J_{3,2}$	%	4.33	10.53	2.18	0.16
Estimation	Time delay	$J_{4,1}$	ms	1.55	20.70	0.00	0.00
		$J_{4,2}$	ms	−0.38	9.58	0.00	0.00
	Normalized estimation error	$J_{5,4}$	%	4.52	16.22	1.96	0.01
		$J_{5,28}$	%	6.20	24.63	1.46	0.05
	Max. peak estimation error	$J_{6,4}$	%	8.54	39.11	2.31	0.19
		$J_{6,28}$	%	14.09	49.43	2.16	0.17

as they correspond to smaller errors in both tracking and global performance.

A total of 1,000 vRTHS simulations were executed to demonstrate the control robustness, each incorporating system uncertainties ($\Delta\boldsymbol{\theta}$) through random variations in the plant parameters (i.e., poles and zeros), which were modeled as normal random variables. Details in generating the above random variations are described in the benchmark problem

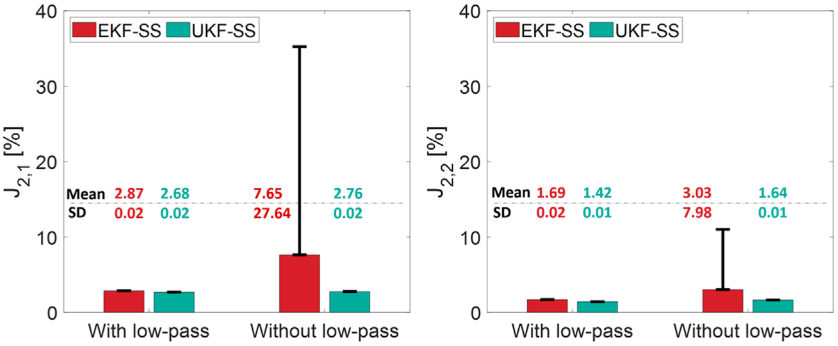

FIGURE 8
Tracking performance criteria for EKF-SS and UKF-SS with and without low-pass filtering.

definition in Condori Uribe et al. (2023). The initial values of the estimated parameters are set to the values of the nominal plant provided in Condori Uribe et al. (2023). All simulations were performed on a personal computer equipped with an Intel Core i7-14700 processor and 64 GB of RAM, running Microsoft Windows 11.

The mean and standard deviation (SD) for each performance indicator (PI) across the four parameter estimation cases using 0.4 scaled El Centro Earthquake as input, are presented in Table 2. Additionally, the results from the linear quadratic regulator (LQR) controller presented in the benchmark (BM) by Condori Uribe et al. (2023) are included in the table for comparison. Results utilizing 0.4 scaled Kobe and 0.4 scaled Morgan earthquakes are presented in the Supplementary Material. Furthermore, Table 3 presents the average simulation time for each earthquake input to evaluate computational efficiency.

The results from Table 2 demonstrate the effectiveness and robustness of the parameter estimation cases for the proposed compensator using the 0.4 scaled El Centro Earthquake as input. The robustness is confirmed by the performance across the 1,000 simulations, which resulted in small PIs with small standard deviations. For time delay, all cases were effective, with the highest mean time delay of 0.47 ms, obtained in the UKF-TF case. The tracking performance was effective in both actuator and frame coordinates ($J_{1,m}$ to $J_{6,m}$) with the largest PIs obtained for the UKF-TF case. For the global RTHS evaluation, all performance estimation cases outperformed the BM-LQG for the degrees of freedom at the control node, although higher errors were obtained at DOFs of the upper levels of the reference structure. Overall, the UKF-SS case exhibited the best tracking performance with PIs values of $J_{2,1} = 2.68 \pm 0.02$ and $J_{2,2} = 1.42 \pm 0.01$ (actuator coordinates), and with $J_{5,4} = 1.82 \pm 0.01$ and $J_{5,28} = 0.85 \pm 0.03$ (frame coordinates). The largest obtained PIs from the 1,000 simulations for the same UKF-SS case were $J_{2,1} = 2.75$ and $J_{2,2} = 1.47$ (actuator coordinates), and with $J_{5,4} = 1.86$ and $J_{5,28} = 0.96$ (frame coordinates). Figure 5 shows the desired and measured displacements in actuator coordinates of actuator 1 for the UKF-SS case with the largest $J_{2,1}$, demonstrating the close match of the signals over time. Similar tracking performance is observed for actuator 2 and for signals in frame coordinates. Therefore, the time history plots for these signals are not included here. Figure 6 illustrates the parameters tracking history (all normalized to the initial nominal values) across the four parameter estimation cases, with the 0.4 scaled El Centro Earthquake as input. This figure demonstrates that meaningful parameter estimation begins around 5 s, when the earthquake input starts (see Figure 5). Parameters continue to update until reaching a stable value to minimize the estimation error. Although starting with the same initial values, the updating histories among the four cases are not consistent. For example, among all the parameters, P_1 shows the largest variation in the EKF cases, with changes of ~ 12% in EKF-SS and ~ 30% in EKF-TF. In contrast, the UKF cases exhibit the largest variations with D_2 (~ 10%) in UKF-SS and with P_2 (~ 2%) in UKF-TF. Figure 7 illustrates the tracking performance of the proposed compensation for all three input earthquakes in both actuator and frame coordinates. The height of each bar represents the mean value of the PI for the respective parameter estimation case, while the error bars indicate one standard deviation (+SD) of the corresponding PI value. Overall, the small PIs values in the bar graph demonstrates the effectiveness and robustness of the compensator across the three earthquake input scenarios. For each earthquake input, the UKF-SS yields the smallest PIs among all compensation cases, while UKF-TF shows the largest PIs and standard deviations, likely due to its less active updating in parameter tracking (see Figure 6D).

Although the UKF-SS shows superior tracking performance compared to the other cases studied, it is also more computationally expensive, as shown in Table 3. This increased computational cost is likely due to the requirement for the UKF algorithm to generate and propagate multiple sigma points, which involves additional matrix operations. Note that, the simulation time indicated in Table 3 is measured during the numerical simulations in MATLAB under Windows environment, not in a real-time computing environment. But by considering the same computational environment, Table 3 can still offer a relative comparison of the computational efficiency of each algorithm.

3.4 Effect of low-pass filter in state-space formulation

Results presented in Section 3.3 are obtained with the use of a 6th-order Butterworth low-pass filter with a cutoff frequency of 20 Hz, applied to $\mathbf{u}_c$ and $\mathbf{x}_m$ (see Figure 3). The low-pass filter helps attenuate high-frequency noise present in the measured signals. This noise is exacerbated during time differentiation when using the TF model, making the use of the low-pass filter crucial to ensure the stability of EKF-TF and UKF-TF cases. In contrast, the discrete-time SS model does not involve time derivatives of the signals and only deals with measurement and process noises. Therefore, the low-pass filter can potentially be removed when using the discrete-time SS model. Table 4 presents the tracking performance PIs ($J_{1,m}$ to $J_{6,m}$) for EKF-SS and UKF-SS cases without low-pass filtering, using 0.4 scaled El Centro earthquake as input in 1,000 simulations. The EKF-SS results, compared to those in Table 2, showed significant decrease in performance, leading to large SDs in Table 4. However, for the UKF-SS case, the obtained PIs are consistent with the values in Table 2, with only a small increase in the PIs. Additionally, Figure 8 shows the bar charts for $J_{2,1}$ and $J_{2,2}$ (values from Tables 2, 4) for the mentioned EKF-SS and UKF-SS cases with and without low-pass filter. The bar height shows the mean PI value, while the error bars indicate one standard deviation (+SD) of the corresponding PI.

These results reveal that UKF can handle noises and nonlinearities in the system model more effectively than EKF when low-pass filter is not present. This capability is advantageous in RTHS because the use of low-pass filter can potentially introduce signal distortion leading to unwanted dynamics with potentially nonlinear systems, and therefore compromise the compensation performance and the accuracy of the simulated response.

4 Conclusion

An adaptive compensation framework for MIMO-RTHS is proposed in this paper. The proposed methodology employs a control law based on the inverse dynamics of the control plant, with adaptive parameters updated in real-time. Parameter estimation utilizes the plant model in TF and discrete-time SS forms, combined with nonlinear parameter estimators EKF and UKF, leading to four proposed estimation cases: EKF-TF, UKF-TF, EKF-SS, and UKF-SS.

The proposed compensation has been examined in a maRTHS benchmark problem, through RTHS simulations incorporating sensor noise, uncertainties in the plant model, and three earthquake inputs. The results for the four parameter estimation cases of the proposed compensation framework showed effective tracking performance at the NS-PS interface node in both actuator and frame coordinates, and strong robustness against uncertainties and noises, with the UKF-SS case exhibiting the best performance in compensation tracking (see Table 2; Figure 7) and robustness against uncertainties and noises (see Table 4; Figure 8). From the implementation of the proposed adaptive compensation, the following additional observations are listed:

- EKF exhibits a higher computational efficiency than UKF, which is reflected by the shorter simulation times of EKF-TF and EFK-SS cases in comparison to UKF-TF and UKF-SS cases (see Table 3). The higher computational complexity of the UKF might pose a challenge in meeting real-time constraints. Therefore, based on the results from Table 3, the EKF-SS case is an efficient choice when the system does not exhibit nonlinearities.
- Utilizing the TF model for parameter estimation (cases EKF-TF and UKF-TF) resulted in a smaller solution space compared to the SS model, but its implementation was more computationally expensive because of the calculations of time derivatives, as indicated by $\gamma_{\mathbf{x}_m}$ in Equation 12.
- From the results in Section 3.4, it is shown that the UKF-SS case maintains good tracking performance without the need of low-pass filtering. Therefore, when RTHS system exhibits strong nonlinearities where low-pass filtering is not suitable, the UKF-SS is the preferred choice due to its robust tracking performance against uncertainties and noises with or without low-pass filtering.
- The implementation of EKF was more involved than UKF, because the high nonlinearity in the system formulations (see Section 2.3) makes the derivation of the Jacobians cumbersome and prone to errors.

The proposed adaptive compensation framework shows significant potential for tracking performance and robustness in MIMO-RTHS. Future research will focus on strengthening the efficiency and robustness of this framework by investigating alternative system formulations and exploring more advanced parameter estimation methods.

Data availability statement

The raw data supporting the conclusions of this article will be made available by the authors, without undue reservation.

Author contributions

SR: Methodology, Data curation, Formal Analysis, Investigation, Software, Visualization, Writing–original draft. WS: Methodology, Conceptualization, Funding acquisition, Project administration, Resources, Supervision, Validation, Writing–review and editing.

Funding

The author(s) declare that financial support was received for the research, authorship, and/or publication of this article. This research was supported by National Science Foundation (NSF) through Grant CMMI 2011423.

Conflict of interest

The authors declare that the research was conducted in the absence of any commercial or financial relationships that could be construed as a potential conflict of interest.

The author(s) declared that they were an editorial board member of Frontiers, at the time of submission. This had no impact on the peer review process and the final decision.

Publisher's note

Supplementary material

The Supplementary Material for this article can be found online at: https://www.frontiersin.org/articles/10.3389/fbuil.2024.1477804/full#supplementary-material

References

Carrion, J. E., Spencer, B. F., and Phillips, B. M. (2009). Real-time hybrid simulation for structural control performance assessment. *Earthq. Eng. Eng. Vib.* 8, 481–492. doi:10.1007/s11803-009-9122-4

Chae, Y., Kazemibidokhti, K., and Ricles, J. M. (2013). Adaptive time series compensator for delay compensation of servo-hydraulic actuator systems for real-time hybrid simulation. *Earthq. Eng. Struct. Dyn.* 42, 1697–1715. doi:10.1002/eqe.2294

Chen, C., and Ricles, J. M. (2009). Analysis of actuator delay compensation methods for real-time testing. *Eng. Struct.* 31, 2643–2655. doi:10.1016/j.engstruct.2009.06.012

Chen, C., Ricles, J. M., Marullo, T. M., and Mercan, O. (2009). Real-time hybrid testing using the unconditionally stable explicit CR integration algorithm. *Earthq. Eng. Struct. Dyn.* 38, 23–44. doi:10.1002/eqe.838

Chen, P.-C., Chang, C.-M., Spencer, B. F., and Tsai, K.-C. (2015). Adaptive model-based tracking control for real-time hybrid simulation. *Bull. Earthq. Eng.* 13, 1633–1653. doi:10.1007/s10518-014-9681-2

Condori Uribe, J. W., Salmeron, M., Patino, E., Montoya, H., Dyke, S. J., Silva, C. E., et al. (2023). Experimental benchmark control problem for multi-axial real-time hybrid simulation. *Front. Built Environ.* 9, 1270996. doi:10.3389/fbuil.2023.1270996

Darby, A. P., Blakeborough, A., and Williams, M. S. (1999). Real-time substructure tests using hydraulic actuator. *J. Eng. Mech.* 125, 1133–1139. doi:10.1061/(ASCE)0733-9399(1999)125:10(1133)

Darby, A. P., Williams, M. S., and Blakeborough, A. (2002). Stability and delay compensation for real-time substructure testing. *J. Eng. Mech.* 128, 1276–1284. doi:10.1061/(ASCE)0733-9399(2002)128:12(1276)

Dyke, S. J., Spencer, B. F., Quast, P., and Sain, M. K. (1995). Role of control-structure interaction in protective system design. *J. Eng. Mech.* 121, 322–338. doi:10.1061/(ASCE)0733-9399(1995)121:2(322)

Gomez, D., Dyke, S., and Maghareh, A. (2014). *Enabling role of hybrid simulation within the NEES infrastructure in advancing earthquake engineering practice and research*. doi:10.13140/2.1.1828.6886

Hayati, S., and Song, W. (2017). An optimal discrete-time feedforward compensator for real-time hybrid simulation. *Smart Struct. Syst.* 20, 483–498. doi:10.12989/SSS.2017.20.4.483

Hayati, S., and Song, W. (2018). Design and performance evaluation of an optimal discrete-time feedforward controller for servo-hydraulic compensation. *J. Eng. Mech.* 144, 04017163. doi:10.1061/(ASCE)EM.1943-7889.0001399

Horiuchi, T., Inoue, M., Konno, T., and Namita, Y. (1999). Real-time hybrid experimental system with actuator delay compensation and its application to a piping system with energy absorber. *Earthq. Eng. Struct. Dyn.* 28, 1121–1141. doi:10.1002/(SICI)1096-9845(199910)28:10<1121::AID-EQE858>3.0.CO;2-O

Huang, W., Ning, X., Ding, Y., and Wang, Z. (2023). A novel actuation dynamics adaptive compensation strategy for real-time hybrid simulation based on unscented kalman filter. *Int. J. Struct. Stab. Dyn.* 23, 2350107. doi:10.1142/S0219455423501079

Julier, S. J. (2002). "The scaled unscented transformation," in Proceedings of the 2002 American Control Conference (IEEE Cat. No.CH37301). Presented at the Proceedings of 2002 American Control Conference, Anchorage, AK, USA, 08-10 May 2002 (IEEE), 4555–4559. doi:10.1109/ACC.2002.1025369

Jung, R.-Y., Benson Shing, P., Stauffer, E., and Thoen, B. (2007). Performance of a real-time pseudodynamic test system considering nonlinear structural response. *Earthq. Eng. Struct. Dyn.* 36, 1785–1809. doi:10.1002/eqe.722

Mathworks (2024). MATLAB. Available at: https://www.mathworks.com/products/matlab.html (Accessed July 27, 2024).

Mercan, O., Ricles, J. M., Sause, R., and Marullo, T. (2009). Kinematic transformations for planar multi-directional pseudodynamic testing. *Earthq. Eng. Struct. Dyn.* 38, 1093–1119. doi:10.1002/eqe.886

Najafi, A., Fermandois, G. A., Dyke, S. J., and Spencer, B. F. (2023). Hybrid simulation with multiple actuators: a state-of-the-art review. *Eng. Struct.* 276, 115284. doi:10.1016/j.engstruct.2022.115284

Nakashima, M., Kato, H., and Takaoka, E. (1992). Development of real-time pseudo dynamic testing. *Earthq. Eng. Struct. Dyn.* 21, 79–92. doi:10.1002/eqe.4290210106

Nakashima, M., and Masaoka, N. (1999). Real-time on-line test for MDOF systems. *Earthq. Eng. Struct. Dyn.* 28, 393–420. doi:10.1002/(SICI)1096-9845(199904)28:4<393::AID-EQE823>3.0.CO;2-C

Ning, X., Wang, Z., Wang, C., and Wu, B. (2022). Adaptive feedforward and feedback compensation method for real-time hybrid simulation based on a discrete physical testing system model. *J. Earthq. Eng.* 26, 3841–3863. doi:10.1080/13632469.2020.1823912

Ning, X., Wang, Z., and Wu, B. (2020). Kalman filter-based adaptive delay compensation for benchmark problem in real-time hybrid simulation. *Appl. Sci.* 10, 7101. doi:10.3390/app10207101

Ouyang, Y., Shi, W., Shan, J., and Spencer, B. F. (2019). Backstepping adaptive control for real-time hybrid simulation including servo-hydraulic dynamics. *Mech. Syst. Signal Process.* 130, 732–754. doi:10.1016/j.ymssp.2019.05.042

Palacio-Betancur, A., and Gutierrez Soto, M. (2019). Adaptive tracking control for real-time hybrid simulation of structures subjected to seismic loading. *Mech. Syst. Signal Process.* 134, 106345. doi:10.1016/j.ymssp.2019.106345

Phillips, B. M., Takada, S., Spencer, B. F., and Fujino, Y. (2014). Feedforward actuator controller development using the backward-difference method for real-time hybrid simulation. *Smart Struct. Syst.* 14, 1081–1103. doi:10.12989/sss.2014.14.6.1081

Silva, C. E., Gomez, D., Maghareh, A., Dyke, S. J., and Spencer, B. F. (2020). Benchmark control problem for real-time hybrid simulation. *Mech. Syst. Signal Process.* 135, 106381. doi:10.1016/j.ymssp.2019.106381

Song, W. (2011). *Dynamic model updating with applications in structural and damping systems: from linear to nonlinear, from off-line to real-time*. PhD Thesis.

Song, W. (2018). Generalized minimum variance unbiased joint input-state estimation and its unscented scheme for dynamic systems with direct feedthrough. *Mech. Syst. Signal Process.* 99, 886–920. doi:10.1016/j.ymssp.2017.06.032

Song, W., and Dyke, S. (2013). Development of a cyber-physical experimental platform for real-time dynamic model updating. *Mech. Syst. Signal Process.* 37, 388–402. doi:10.1016/j.ymssp.2012.12.007

Song, W., and Dyke, S. (2014). Real-time dynamic model updating of a hysteretic structural system. *J. Struct. Eng.* 140, 04013082. doi:10.1061/(ASCE)ST.1943-541X.0000857

Song, W., Hayati, S., and Zhou, S. (2017). Real-time model updating for magnetorheological damper identification: an experimental study. *Smart Struct. Syst.* 20, 619–636. doi:10.12989/SSS.2017.20.5.619

Song, W., Sun, C., Zuo, Y., Jahangiri, V., Lu, Y., and Han, Q. (2020). Conceptual study of a real-time hybrid simulation framework for monopile offshore wind turbines under wind and wave loads. *Front. Built Environ.* 6, 129. doi:10.3389/fbuil.2020.00129

Strano, S., and Terzo, M. (2016). Actuator dynamics compensation for real-time hybrid simulation: an adaptive approach by means of a nonlinear estimator. *Nonlinear Dyn.* 85, 2353–2368. doi:10.1007/s11071-016-2831-0

Wan, E. A., and Van Der Merwe, R. (2000). "The unscented Kalman filter for nonlinear estimation," in Proceedings of the IEEE 2000 Adaptive Systems for Signal Processing, Communications, and Control Symposium (Cat. No.00EX373). Presented at the Symposium on Adaptive Systems for Signal Processing Communications and Control, Lake Louise, Alta., Canada, 04-04 October 2000 (IEEE), 153–158. doi:10.1109/ASSPCC.2000.882463

Wang, T., Gong, Y., Xu, G., and Wang, Z. (2024). Unscented kalman filter-based two-stage adaptive compensation method for real-time hybrid simulation. *J. Earthq. Eng.* 28, 3221–3255. doi:10.1080/13632469.2024.2335346

Wang, Z., Guoshan, X., Qiang, L., and Bin, W. (2020). An adaptive delay compensation method based on a discrete system model for real-time hybrid simulation. *SMART Struct. Syst.* doi:10.12989/sss.2020.25.5.569

Zhao, J., French, C., Shield, C., and Posbergh, T. (2003). Considerations for the development of real-time dynamic testing using servo-hydraulic actuation. *Earthq. Eng. Struct. Dyn.* 32, 1773–1794. doi:10.1002/eqe.301